Image restoration for ring-array photoacoustic tomography system based on blind spatially rotational deconvolution

Wende Dong [a,b], Chenlong Zhu [a,b], Dan Xie [c], Yanli Zhang [a,b], Shuyin Tao [d], Chao Tian [c,e,f,*]

[a] College of Automation Engineering, Nanjing University of Aeronautics and Astronautics, Nanjing, Jiangsu 211106, China
[b] Key Laboratory of Space Photoelectric Detection and Perception (Nanjing University of Aeronautics and Astronautics), Ministry of Industry and Information Technology, Nanjing, Jiangsu 211106, China
[c] School of Engineering Science, University of Science and Technology of China, Hefei, Anhui 230026, China
[d] School of Computer Science and Engineering, Nanjing University of Science and Technology, Nanjing, Jiangsu 210094, China
[e] Institute of Artificial Intelligence, Hefei Comprehensive National Science Center, Hefei, Anhui 230088, China
[f] Anhui Province Key Laboratory of Biomedical Imaging and Intelligent Processing, Institute of Artificial Intelligence, Hefei Comprehensive National Science Center, Hefei, Anhui 230088, China

ARTICLE INFO

ABSTRACT

Ring-array photoacoustic tomography (PAT) system has been widely used in noninvasive biomedical imaging. However, the reconstructed image usually suffers from spatially rotational blur and streak artifacts due to the non-ideal imaging conditions. To improve the reconstructed image towards higher quality, we propose a concept of spatially rotational convolution to formulate the image blur process, then we build a regularized restoration problem model accordingly and design an alternating minimization algorithm which is called blind spatially rotational deconvolution to achieve the restored image. Besides, we also present an image preprocessing method based on the proposed algorithm to remove the streak artifacts. We take experiments on phantoms and in vivo biological tissues for evaluation, the results show that our approach can significantly enhance the resolution of the image obtained from ring-array PAT system and remove the streak artifacts effectively.

1. Introduction

Photoacoustic tomography (PAT) is a rapidly developing imaging modality and has been used in a range of biomedical fields [1,2]. A typical PAT system uses nanosecond laser pulses to illuminate biological tissues, which causes a pulse temperature rise and leads to ultrasound emission due to the thermoelastic effect. The emitted acoustic signal is recorded by ultrasound transducer array and used to reconstruct the optical absorption map with certain algorithms, e.g., the time reversal (TR) [3,4], filtered back projection (FBP) [5,6], and model based iterative algorithms [7,8]. Many studies have shown that the PAT can achieve rich optical contrast and high ultrasonic resolution, which makes it a great potential choice for biomedical and clinical applications [9,10].

Ultrasound transducer array is the main part of PAT system and there are different geometries of it, such as linear, cylindrical, and spherical, etc., among which the ring-shaped transducer array is very widely used because of its compact structure and rotationally symmetric imaging property. However, the problem is that most of the reconstruction algorithms are derived from ideal imaging conditions, e.g., the elements of the transducer array should have a point-like aperture and infinite bandwidth. The real PAT system cannot meet these requirements and results in inevitable degradation of image quality. Especially for the PAT system with a ring-shaped transducer array, the reconstructed images evidently suffer from spatially rotational blur, which means as the distance from the center of the PAT system increases, the resolution degrades more and more seriously along the tangential direction. Besides, for the real PAT system with insufficient number of transducers, the reconstruction methods such as the FBP based algorithms usually result in streak artifacts in the reconstructed images [11]. Both of the two undesired artifacts significantly degrade the performance of ring-array PAT system, thus it is of very important meaning for restoring the reconstructed image towards higher resolution and less streak artifacts.

Deconvolution methods aim to estimate the clear image from the blurred. Roughly, it can be divided into two categories, i.e., non-blind and blind image deconvolution. In non-blind image deconvolution, the

---

Point Spread Function (PSF) is measured in advance with some auxiliary methods, we only need to estimate the clear image. Whereas in blind deconvolution, both the PSF and clear image needs to be estimated. Just like most inverse problems, both of the two kinds of deconvolutions are ill-posed, which means the restored image tends to be contaminated by undesired artifacts such as amplified noise. Regularization is the most commonly used method to alleviate ill-posedness, which introduces additional constraints into the original inverse problem to formulate a more stable problem model to suppress the undesired artifacts, and there have been many deconvolution methods based on total variation (TV) [12–14], Tikhonov [15–17], hyper-Laplacian [18–20], and L_0-norm [21–25] regularizations. However, most of the existing researches are only suitable for handling spatially invariant blur, i.e., the PSF is identical for all the pixels. Although there are deconvolution methods for restoring spatially variant blurred images [26–31], some of them adopt complex auxiliary equipment to measure and reconstruct the PSF for every pixel [26,27], while others are built on very complicated models and of very low efficiency [28–31], all of them are not suitable for dealing with the spatially rotational blur accompanied with the ring-array PAT system.

To our knowledge, there have been some researches that adopt deconvolution methods to improve the performance of PAT system. For example, some of them deconvolve the recorded PA signals with either spatial impulse response (SIR) [32,33] or electrical impulse response (EIR) [34,35] to enhance the resolution. In [36,37], the authors propose a deconvolution based reconstruction method, which models the recorded signals as the convolution of the optical absorption map and the impulse response of the PAT system. Finally, it uses non-blind deconvolution to recover the absorption map. In [38,39], the total impulse response (TIR) is incorporated with the model-based iterative reconstruction algorithm to improve the image resolution, which can be regarded as a special kind of deconvolution method. Deconvolution methods are also used for postprocessing in image domain, e.g., the methods in [40–43] adopt blind deconvolution for PAT image restoration, but they also assume the PSF is spatially invariant. In [44], the authors propose a non-blind spatially variant deconvolution method to improve the resolution of PAT image, they first use acoustic absorbing microspheres to measure the spatially variant PSFs at preset positions in the PAT system, then they get the PSFs of all the other pixels with a multi-Gaussian based fitting method and bilinear interpolation, the degraded PAT image is finally restored with the hyper-Laplacian regularized non-blind deconvolution method [19]. Recently, our research group has also proposed a similar non-blind spatially variant deconvolution approach as that in [44], which is derived by combining the Poisson distribution with a novel sparse logarithmic gradient regularization term [45]. Experimental results show that both of the two methods in [44] and [45] are very effective in improving the quality of PAT images.

For streak artifacts suppression, the model based reconstruction methods can produce PAT images with weak streak artifacts, but at the cost of large computational burden and memory demand. Just like deconvolution, they also need the assistance of regularizations, such as the L_1-norm of image gradients and TV [46–49]. There are also some streak artifacts suppression methods based on modified back projection (BP) algorithms, e.g., in [50], the authors analyze the property of back projection path in the detection region and present special weight functions to reduce the undesired artifacts in BP algorithms. In [51], a modified BP algorithm named Contamination Tracing Back Projection (CTBP) is proposed for the mitigation of streak artifacts, which can adaptively adjust the back-projection weight according to the likelihood of contamination. However, how to balance the preservation of useful image details and the suppression of the streak artifacts is still a challenging task for these methods.

In recent years, the deep learning based methods have also been widely used for postprocessing PAT images [52], e.g., in [53–56], different U-shaped neural networks (U-net) are adopted to remove the

artifacts caused by sparse-view or limited-view reconstruction. While in [57–59], the framework of generative adversarial network (GAN) is adopted to improve the image quality. Specifically, the research in [57] uses Wasserstein GAN with gradient penalty to mitigate the artifacts caused by the limited-view and limited-bandwidth detection data. In [58] and [59], two variants of GAN i.e., the ResGAN and LV-GAN are developed to enhance the quality of the reconstructed image. Besides, deep learning based methods are also developed to deal with other imaging problems in PAT, such as suppressing the reflection artifacts [60], eliminating the need for radius calibration [61], or correcting speed of sound aberration in a heterogeneous media [62]. To our knowledge, there are few researches focusing on using deep learning to simultaneously remove the spatially variant blur and streak artifacts in PAT images. Only in [63], the authors propose an unsupervised learned network that aims to extract the spatially variant PSFs and clear image from the degraded PAT image. However, just like the methods in [44] and [45], the network still needs some pre-measured PSFs to alleviate the ill-posedness and avoid converging to unsatisfactory results.

In this paper, we aim to design a concise and efficient approach to remove the spatially rotational blur and streak artifacts simultaneously from the images obtained by a ring-array PAT system. In [64] and [65], the authors have explained the reasons for resolution degradation in PAT systems, and based on their analysis, we propose a new concept called spatially rotational convolution to describe the spatially rotational blur due to the size of the transducer element in a ring-array PAT system, i.e., it is modeled by rotating the clear image with several equally spaced degrees and calculating the weighted sum of them. Then based on it, we derive an image deconvolution problem model which takes TV [12–14] as regularization to suppress the undesired artifacts emerging in the restoration process. We further propose an efficient alternating minimization algorithm called blind spatially rotational deconvolution which can estimate the clear image and weights of each rotation from the deconvolution problem model. Additionally, if the weights are known, we call it non-blind spatially rotational deconvolution.

Based on the algorithm, we design a two stage restoration approach to achieve the final result. The first stage is image preprocessing, just like in [45], we analyze the approximately periodic property of the streak artifacts and propose a method based on the non-blind spatially rotational deconvolution algorithm to remove it. In the second stage, we adopt the blind spatially rotational deconvolution method to estimate the weights for the rotations in the degradation model and achieve the final restored image. We evaluate our approach with experiments on phantoms and in vivo biological tissues, the restoration results show that it can significantly enhance the resolution of the reconstructed images and remove the streak artifacts effectively, the image quality is obviously improved.

The superiority of our approach is that there is no need to measure and reconstruct the spatially variant PSFs with auxiliary equipment as some state of the art methods [44,45,63]. Therefore, it is much more convenient to be used to improve the quality of PAT images obtained from different ring-array PAT systems.

The rest of the paper is organized as follows: Section 2 presents the proposed method including problem formulation, optimization approach and the image preprocessing method. Section 3 shows the experimental results of phantoms and in vivo biological tissues. Section 4 presents some necessary discussions. Finally, a conclusion is made in Section 5.

2. Methodology

2.1. Problem formulation

In [64] and [65], the authors have proven that the images obtained from PAT systems usually suffer from spatially variant blur, which is determined by many factors such as the central detection frequency,

bandwidth, shape of individual element, and the spatial arrangement of the elements. The traditional mathematical model for spatially variant blur is pixel-wise as shown in the following equation:

$$\mathbf{y}_i = (\mathbf{h}_i * \mathbf{x})_i + \mathbf{n}_i \tag{1}$$

where $\mathbf{x}$, $\mathbf{y}$, and $\mathbf{n}$ represent the clear image of the absorption map, reconstructed PAT image, and measurement error, respectively. $i = 1, 2, \cdots, M$ denotes the pixel index and M is the total number of pixels. $\mathbf{h}_i$ represents the PSF corresponding to pixel $\mathbf{x}_i$ and $*$ is the convolution operator.

We can see from Eq. (1) that even if the image $\mathbf{x}$ and all $\mathbf{h}_i$ are of small sizes, there will be a huge gap between the numbers of unknown variables and known data. For example, if the size of $\mathbf{x}$ is 256×256 and the size of each $\mathbf{h}_i$ is 10×10, then the total number of unknown variables is 256×256+256×256×10×10 ($\mathbf{n}$ is a random variable that is not need to be estimated), whereas the number of known pixel data in $\mathbf{y}$ is only 256×256, the ratio between them is 101, thus the deconvolution process is severely ill-posed, which means it will be very difficult to accurately estimate $\mathbf{x}$ and all $\mathbf{h}_i$ from $\mathbf{y}$. Therefore, in recent researches, the authors have to adopt auxiliary devices to measure and calculate the PSFs of all the pixels, then the degraded PAT image is restored with certain regularized non-blind deconvolution algorithms [44,45]. However, since $\mathbf{h}_i$ is different from one another that limits the application of acceleration strategies such as the fast Fourier transform, the restoration process is very time-consuming. Therefore, it is very necessary to design a convenient and efficient method for PAT image restoration.

In the PAT system with a ring-shaped transducer array, the image blur mainly appears spatially rotational due to the size of the transducer element. To formulate it more concisely, we propose the concept of spatially rotational convolution, i.e., we assume that the rotational blur caused by the size of the transducer element in a ring-array PAT system is generated by rotating the clear image with several equally spaced degrees and calculating the weighted sum of them. To describe the concept mathematically, we first define a small degree interval $\Delta\theta$, e.g., $\Delta\theta = 0.01°$, a rotation degree set $\boldsymbol{\theta} = [-N\Delta\theta, \cdots, j\Delta\theta, \cdots, N\Delta\theta]$, and a weight vector $\mathbf{w} = [w_{-N}, \cdots, w_j, \cdots, w_N]$, where $j = -N, \cdots, 0, \cdots, N$ denotes the rotation index and N is a constant, e.g., $N = 1000$. For simplicity, we call $\mathbf{w}$ the spatially rotational PSF, and to satisfy the energy conservation requirement during the blur process, all the elements in $\mathbf{w}$ should be nonnegative and the sum of them equals to 1. Then we define a rotation operator $\mathbf{R}_{j\Delta\theta}$ that $\mathbf{R}_{j\Delta\theta}\mathbf{x}$ means rotating $\mathbf{x}$ by the degree of $j\Delta\theta$. With these definitions, the expression of spatially rotational convolution can be formulated by

$$\mathbf{y} = \sum_{j=-N}^{N} w_j \mathbf{R}_{j\Delta\theta}\mathbf{x} \tag{2}$$

Based on Eq. (2), the complete spatially rotational blur process can be modeled by

$$\mathbf{y} = \sum_{j=-N}^{N} w_j \mathbf{R}_{j\Delta\theta}\mathbf{x} + \mathbf{n} \tag{3}$$

Here, we define $N\Delta\theta$ as the largest rotation degree of the blur extent, and according to the theory in [64] and [65], we can get that it equals to half the degree of the transducer element with respect to the center of the ring array, just as shown in Fig. 1. In real ring-array PAT systems, the transducer arrays usually contain 64, 128, 256, or 512 elements, thus we can calculate that the corresponding largest rotation degrees are 360°/64/2≈2.81°, 360°/128/2=1.41°, 360°/256/2=0.70°, and 360°/512/2=0.35°, respectively. Strictly, all the imaging parameters including the number of transducer elements are unknown in blind deconvolution, when we initialize the algorithm, the largest rotation degree should be set no smaller than all of the above degrees to ensure that the algorithm works well for most real ring-array PAT systems, thus we set it to be 3°, i.e., $N\Delta\theta = 3°$. We can also set it larger than 3°, such as

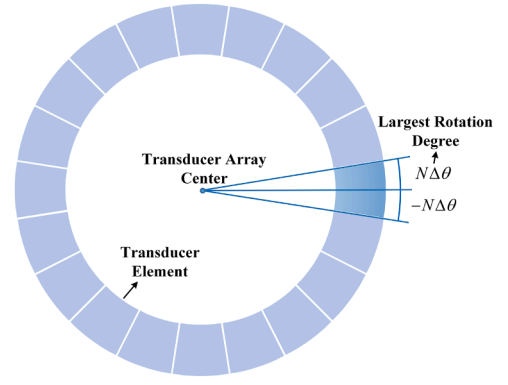**Fig. 1.** Schematic diagram of the largest rotation degree $N\Delta\theta$.

4° or 5°, but the computational burden of the algorithm will be heavier. We also find that $\Delta\theta = 0.01°$ is small enough to produce a high-quality spatially rotational blurred image, thus we can get $N = 3°/0.01° = 300$. Then the total number of unknown variables in Eq. (3) is 256×256+2×300+1, and the ratio between it and the number of known pixel data is 1.01. Both of them are much smaller than that of Eq. (1), which means the deconvolution process of Eq. (3) is much more stable and it will be much easier to achieve an accurate estimation of $\mathbf{x}$ and $\mathbf{w}$ from $\mathbf{y}$.

Then with the least square method, we can obtain a preliminary blind image deconvolution problem model as follow, i.e.,

$$(\mathbf{x}, \mathbf{w}) = \operatorname{argmin}_{(\mathbf{x}, \mathbf{w})} \left\| \sum_{j=-N}^{N} w_j \mathbf{R}_{j\Delta\theta}\mathbf{x} - \mathbf{y} \right\|_2^2 \tag{4}$$

However, it is known that blind image deconvolution is a severely ill-posed problem, if there is no regularization term, the result tends to be contaminated by a lot of undesired artifacts. Therefore, we introduce two regularization terms to constrain the estimations of $\mathbf{x}$ and $\mathbf{w}$, respectively. Then the problem is reformulated as follow:

$$(\mathbf{x}, \mathbf{w}) = \operatorname{argmin}_{(\mathbf{x}, \mathbf{w})} \frac{\lambda}{2} \left\| \sum_{j=-N}^{N} w_j \mathbf{R}_{j\Delta\theta}\mathbf{x} - \mathbf{y} \right\|_2^2 + L(\mathbf{x}) + \frac{\sigma}{2} Q(\mathbf{w}) \tag{5}$$

where $L(\mathbf{x})$ and $Q(\mathbf{w})$ are the regularization terms for $\mathbf{x}$ and $\mathbf{w}$, respectively. λ and σ are the regularization coefficients.

There have been many regularization methods which can be used to construct the term $L(\mathbf{x})$, e.g., the classic TV regularization [13], Tikhonov regularization [17], and hyper-Laplacian regularization [19], etc. Since the TV regularization performs well in preserving image edges and details, and the resulted optimization problem is of relatively low complexity, we use it to model $L(\mathbf{x})$, the expression is given by

$$L(\mathbf{x}) = TV(\mathbf{x}) = \sum_{i=1}^{M} \sqrt{(\mathbf{d}_h\mathbf{x})_i^2 + (\mathbf{d}_v\mathbf{x})_i^2} \tag{6}$$

where $\mathbf{d}_h$ and $\mathbf{d}_v$ are the horizontal and vertical difference operators. In addition, to avoid too complicated optimization problem, we use the basic Tikhonov regularization to model $Q(\mathbf{w})$, i.e.,

$$Q(\mathbf{w}) = \|\mathbf{w}\|_2^2 \tag{7}$$

Then we incorporate Eqs. (5), (6), and (7), the proposed blind spatially rotational deconvolution problem model is finally given by

$$(\mathbf{x}, \mathbf{w}) = \operatorname{argmin}_{(\mathbf{x}, \mathbf{w})} \frac{\lambda}{2} \left\| \sum_{j=-N}^{N} w_j \mathbf{R}_{j\Delta\theta}\mathbf{x} - \mathbf{y} \right\|_2^2 + \sum_{i=1}^{M} \sqrt{(\mathbf{d}_h\mathbf{x})_i^2 + (\mathbf{d}_v\mathbf{x})_i^2} + \frac{\sigma}{2} \|\mathbf{w}\|_2^2 \tag{8}$$

2.2. Optimization approach

We propose an alternating minimization approach called blind spatially rotational deconvolution to solve the problem in Eq. (8). Firstly, we divide it into two sub-problems which are shown in Eq. (9) and Eq. (10). For simplicity, we call them **x**-problem and **w**-problem, respectively.

x-problem: fix **w** and estimate **x**, i.e.,

$$\mathbf{x} = \operatorname{argmin}_{\mathbf{x}} \frac{\lambda}{2} \left\| \sum_{j=-N}^{N} w_j \mathbf{R}_{j\Delta\theta} \mathbf{x} - \mathbf{y} \right\|_2^2 + \sum_{i=1}^{M} \sqrt{(\mathbf{d}_h \mathbf{x})_i^2 + (\mathbf{d}_v \mathbf{x})_i^2} \tag{9}$$

w-problem: fix **x** and estimate **w**, i.e.,

$$\mathbf{w} = \operatorname{argmin}_{\mathbf{w}} \frac{\lambda}{2} \left\| \sum_{j=-N}^{N} w_j \mathbf{R}_{j\Delta\theta} \mathbf{x} - \mathbf{y} \right\|_2^2 + \frac{\sigma}{2} \|\mathbf{w}\|_2^2 \tag{10}$$

According to the optimization theory, the solution of Eq. (8) can be reached by alternately solving the **x**-problem and **w**-problem until convergence. In the following subsections, we will show how to efficiently achieve the solutions of the above two sub-problems.

2.2.1. The method for solving the x-problem

The **x**-problem is a complicated non-quadratic optimization problem, we propose to adopt the variable splitting and quadratic penalty method to solve it. Firstly, we introduce a penalty coefficient β and an auxiliary variable **u** to approximate the variable **x** in the TV term and convert Eq. (9) into Eq. (11). Based on the principal of quadratic penalty method, as $\beta \to +\infty$, the solution of Eq. (11) converges to that of Eq. (9).

$$\left(\mathbf{x}, \mathbf{u} \right) = \operatorname{argmin}_{(\mathbf{x}, \mathbf{u})} \frac{\lambda}{2} \left\| \sum_{j=-N}^{N} w_j \mathbf{R}_{j\Delta\theta} \mathbf{x} - \mathbf{y} \right\|_2^2 + \frac{\beta}{2} \|\mathbf{x} - \mathbf{u}\|_2^2 + \sum_{i=1}^{M} \sqrt{(\mathbf{d}_h \mathbf{u})_i^2 + (\mathbf{d}_v \mathbf{u})_i^2} \tag{11}$$

The problem in Eq. (11) can be solved by alternately implementing the following three steps until β reaching a large value $\beta_{\max}$.

Step 1: fix **x** and solve for **u**, i.e.,

$$\mathbf{u} = \operatorname{argmin}_{\mathbf{u}} \frac{\beta}{2} \|\mathbf{x} - \mathbf{u}\|_2^2 + \sum_{i=1}^{M} \sqrt{(\mathbf{d}_h \mathbf{u})_i^2 + (\mathbf{d}_v \mathbf{u})_i^2} \tag{12}$$

Step 2: fix **u** and solve for **x**, i.e.,

$$\mathbf{x} = \operatorname{argmin}_{\mathbf{x}} \frac{\lambda}{2} \left\| \sum_{j=-N}^{N} w_j \mathbf{R}_{j\Delta\theta} \mathbf{x} - \mathbf{y} \right\|_2^2 + \frac{\beta}{2} \|\mathbf{x} - \mathbf{u}\|_2^2 \tag{13}$$

Step 3: update β, i.e.,

$$\beta = \beta r \quad (r > 1) \tag{14}$$

The problem in Eq. (12) is a standard TV denoising problem and there have been many efficient algorithms to solve it, in this paper, we choose the method in [66]. Eq. (13) is a quadratic optimization problem with respect to **x**, which can be solved by setting the derivative of its cost function to zero. To make the expression more concise, we introduce an operator **A** to represent the rotation and weighted sum operation of **x** given **w**, i.e.,

$$\mathbf{A}\mathbf{x} = \sum_{j=-N}^{N} w_j \mathbf{R}_{j\Delta\theta} \mathbf{x} \tag{15}$$

then Eq. (13) is converted into the following expression:

$$\mathbf{x} = \operatorname{argmin}_{\mathbf{x}} \frac{\lambda}{2} \|\mathbf{A}\mathbf{x} - \mathbf{y}\|_2^2 + \frac{\beta}{2} \|\mathbf{x} - \mathbf{u}\|_2^2 \tag{16}$$

Denote the cost function in Eq. (16) as $J(\mathbf{x})$, i.e.,

$$J(\mathbf{x}) = \frac{\lambda}{2} \|\mathbf{A}\mathbf{x} - \mathbf{y}\|_2^2 + \frac{\beta}{2} \|\mathbf{x} - \mathbf{u}\|_2^2 \tag{17}$$

with $dJ(\mathbf{x})/d\mathbf{x} = \mathbf{0}$, we can get

$$\left(\lambda \mathbf{A}^T \mathbf{A} + \beta \mathbf{I} \right) \mathbf{x} = \lambda \mathbf{A}^T \mathbf{y} + \beta \mathbf{u} \tag{18}$$

where **I** is the identity matrix and $\mathbf{A}^T$ denotes the adjoint operator of **A**, i. e.,

$$\mathbf{A}^T \mathbf{x} = \sum_{j=-N}^{N} w_j \mathbf{R}_{-j\Delta\theta} \mathbf{x} \tag{19}$$

Generally, the solution of Eq. (18) can be obtained by taking the inversion of the left part, i.e.,

$$\mathbf{x} = \left(\lambda \mathbf{A}^T \mathbf{A} + \beta \mathbf{I} \right)^{-1} \left(\lambda \mathbf{A}^T \mathbf{y} + \beta \mathbf{u} \right) \tag{20}$$

However, from the definitions of **A** and $\mathbf{A}^T$ we know that they contain many rotation operations, which makes them difficult to be represented by matrices, thus Eq. (20) is invalid. Instead, we use the conjugate gradient (CG) method to solve for **x** in Eq. (18).

Additionally, we can see that the above method for solving the **x**-problem is essentially a non-blind spatially rotational deconvolution method.

2.2.2. The method for solving the w-problem

To solve the **w**-problem, we should first construct a matrix **B** whose definition is given by

$$\mathbf{B} = \left[\mathbf{R}_{-N\Delta\theta} \mathbf{x}_1, \cdots, \mathbf{R}_{j\Delta\theta} \mathbf{x}, \cdots, \mathbf{R}_{N\Delta\theta} \mathbf{x} \right] \tag{21}$$

then the **w**-problem in Eq. (10) is simplified to

$$\mathbf{w} = \operatorname{argmin}_{\mathbf{w}} \frac{\lambda}{2} \|\mathbf{B}\mathbf{w} - \mathbf{y}\|_2^2 + \frac{\sigma}{2} \|\mathbf{w}\|_2^2 \tag{22}$$

Similar to the method for solving Eq. (16), we denote its cost function as

$$J(\mathbf{w}) = \frac{\lambda}{2} \|\mathbf{B}\mathbf{w} - \mathbf{y}\|_2^2 + \frac{\sigma}{2} \|\mathbf{w}\|_2^2 \tag{23}$$

take the derivative of $J(\mathbf{w})$ and set it to zero, then we can get

$$\mathbf{w} = \left(\lambda \mathbf{B}^T \mathbf{B} + \sigma \mathbf{I} \right)^{-1} \lambda \mathbf{B}^T \mathbf{y} \tag{24}$$

In order to keep the energy during the deconvolution process, after **w** is calculated, all its elements should be normalized by

$$w_i = \max(w_i, 0) \Big/ \sum_{i=1}^{M} \max(w_i, 0) \tag{25}$$

where $\max(w_i, 0)$ represents the maximum value of w_i and 0.

In summary, we show the main steps of the proposed blind spatially rotational deconvolution method in Algorithm 1, where k and $k_{\max}$ denote the index and total number of alternating minimization

iterations of Eq. (9) and Eq. (10), respectively.

Algorithm 1. The main algorithmic steps of the proposed method

1.	Initialization: λ, σ, β, r, $\mathbf{w}$, $\mathbf{x} = \mathbf{y}$, $\mathbf{u} = \mathbf{0}$
2.	While $k < k_{\max}$
3.	While $\beta < \beta_{\max}$
4.	Solving Eq. (12) with the method in [66]
5.	Solving Eq. (18) with CG method
6.	$\beta = \beta r$ $(r > 1)$
7.	End
8.	Solving Eq. (22) and normalized $\mathbf{w}$ with Eq. (25).
9.	End
10.	Output: $\mathbf{x}$, $\mathbf{w}$

From the above descriptions, we can summarize the advantages of the proposed algorithm as follows: with the alternating minimization scheme, the original complicated blind spatially rotational deconvolution problem in Eq. (8) is converted into a non-blind spatially rotational deconvolution problem (the $\mathbf{x}$-problem) and a simple quadratic optimization problem (the $\mathbf{w}$-problem), whose difficulty is significantly reduced. Then with the variable splitting and quadratic penalty method, the $\mathbf{x}$-problem is further transformed to a much easier denoising problem (i.e., Eq. (12)) and a quadratic optimization problem (i.e., Eq. (13)). Therefore, the proposed algorithm can solve the blind spatially rotational deconvolution problem very efficiently.

2.3. Image preprocessing

Due to the limited number of elements in the transducer array, the PAT images reconstructed from the under-sampled data are usually contaminated by streak artifacts, especially in in vivo experiments where the photoacoustic absorbers have stronger optical absorption than their backgrounds. Since our goal is to achieve a restored image with clear details and few undesired artifacts, we also propose an image preprocessing method to remove most of the streak artifacts.

Just as mentioned in Section 1, some of the existing methods depend on regularization to suppress the streak artifacts, but it is difficult for these methods to distinguish the image details and streak artifacts in the restoration process. Fortunately, we find out that the streak artifacts in the PAT images obtained from a ring-shaped transducer array are approximately periodic, and the period is determined by the structure of the ring-array PAT system. If we rotate it around the image center with certain degree, then superimpose and calculate the average image of them, the peaks and valleys of the streak artifacts will cancel each other out [45]. In practice, we rotate the PAT image clockwise and counter-clockwise once each and calculate the average image to guarantee effective suppression of the streak artifacts. The expression is given as follow:

$$\mathbf{x}_{average} = \frac{1}{4}\left(\mathbf{x} + \mathbf{R}_{-\theta_0}\mathbf{x} + \mathbf{x} + \mathbf{R}_{\theta_0}\mathbf{x}\right) \tag{26}$$

where $\mathbf{x}_{average}$ denotes the average image, and θ_0 is the rotation degree for suppressing the streak artifacts. In practice, we tune the value of θ_0 gradually and calculate the average image according to Eq. (26), when

the streak artifacts in the average image is the weakest, the value of θ_0 is found. With this method, we get that the value of θ_0 is about $1°$ for our experimental system. Since θ_0 is related to the period of the streak artifacts, it is also determined by the structure of the ring-array PAT system, and it can be used to preprocess all the images obtained from the same system.

Furthermore, Eq. (26) can be recast to into the following equation:

$$\mathbf{x}_{average} = \frac{1}{2}\mathbf{R}_0\mathbf{x} + \frac{1}{4}\mathbf{R}_{-\theta_0}\mathbf{x} + \frac{1}{4}\mathbf{R}_{\theta_0}\mathbf{x} \tag{27}$$

It is evident that Eq. (27) is of the same form as Eq. (2), which means the above operation is essential a spatially rotational convolution process: the set of rotation degrees is $[-\theta_0, 0, \theta_0]$ and the corresponding spatially rotational PSF $\mathbf{w}$ is $[1/4, 1/2, 1/4]$, thus we can use the non-blind spatially rotational deconvolution algorithm to deconvolve $\mathbf{x}$ from $\mathbf{x}_{average}$. Since the peaks and valleys of the streak artifacts have canceled each other out, their energy disappears, they will not appear again in the deconvolved image. Fig. 2 shows an example of pre-processing a PAT image, where Fig. 2(a) is the original PAT image of a human finger reconstructed by the FBP algorithm, Fig. 2(d) is the enlarged view of the contents in the red rectangle in Fig. 2(a), we can see that there are evident streak artifacts in the backgrounds which are indicated by the white arrow, and some of them invades the main part of the image as pointed by the yellow arrow. Fig. 2(b) is the output of Eq. (27) and Fig. 2(e) is the enlarged view of the contents in the red rectangle in Fig. 2(b), we can see that the streak artifacts are removed and the image becomes slightly more blurred due to the operation of Eq. (27). Fig. 2(c) is the deconvolved image and Fig. 2(f) shows the locally enlarged contents in the red rectangle of Fig. 2(c), we can see that the image becomes clearer and there are few streak artifacts.

After preprocessing the reconstructed PAT image with the above approach, we use the proposed blind spatially rotational deconvolution algorithm to further remove the spatially rotational blur and obtain the final restored image.

2.4. Parameter setting

Based on the above analysis as well as many simulations and experiments, in the stage of blind deconvolution, we set $\Delta\theta = 0.01°$, $N = 300$ and initialize all the elements in the spatially rotational PSF $\mathbf{w}$ with $1/N$, we empirically tune λ and σ in the ranges of $100 \leq \lambda \leq 500$ and $100\lambda \leq \sigma \leq 50000\lambda$, respectively. The penalty coefficient β is initialized with 1 and increased by a factor $r = 2$ until it reaches $\beta_{\max} = 2^{12}$. While in the stage of image preprocessing, we empirically set $\theta_0 = 1°$, $\lambda = 1500$, and $\beta_{\max} = 2^{15}$, the updating scheme of β is kept unchanged.

3. Experiments

3.1. Experimental setup

We adopt PAT images of some phantoms and in vivo biological tissues to verify the effectiveness of the proposed method, all of which are obtained from the same experimental setup: the radius of the ring-shaped transducer array is 25 mm which has 256 unfocused elements with flat rectangular aperture, the size of each element is 0.51 mm and the space between them is 0.1 mm, the wavelength of the laser is fixed at 750 nm, the center frequency and bandwidth of the array is 7 MHz and 73%, respectively. The speed of sound v_s in the medium is about 1500 m/s, and the reconstruction method is the FBP algorithm.

In addition, although there have been some spatially invariant deconvolution methods which are designed for restoring PAT images [40–43], they are obviously unsuitable for dealing with the spatially variant blur concerned by this paper, thus we do not use them for comparison. Instead, we choose to compare our approach with a state of the art non-blind spatially variant deconvolution method for PAT image restoration [44], but with some necessary modifications on it as follow.
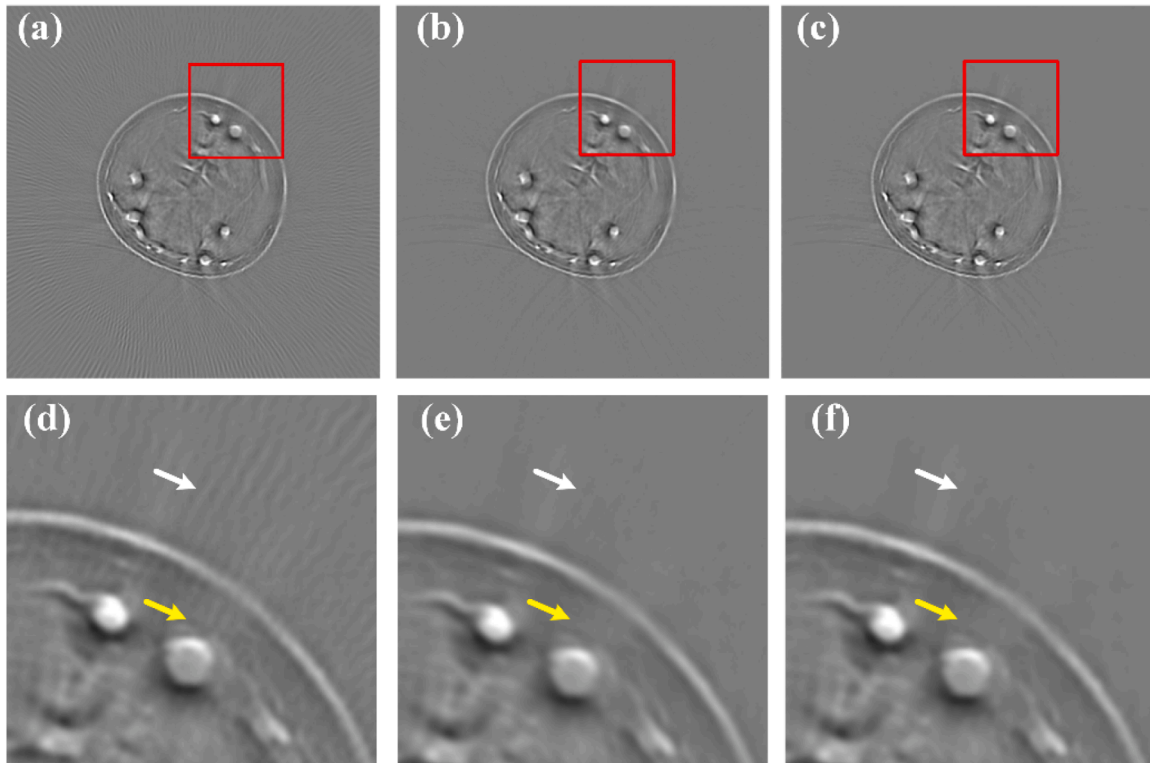
Fig. 2. Streak artifacts suppression with the proposed image preprocessing method. (a) The original PAT image of a human finger reconstructed by the FBP algorithm. (b) The average image obtained with Eq. (27). (c) The deconvolved image of (b). (d)-(f) The enlarged views of the contents in the red rectangles in (a)-(c), respectively.

In [44], the authors design a device to measure the PSFs of some preset pixels in the PAT image, then they use the multi-Gaussian function to model the measured PSFs, and adopt bilinear interpolation to obtain the PSFs for all the other pixels. After that, the blurred PAT image is restored with the non-blind deconvolution method based on sparse hyper-Laplacian regularization [19]. However, there is something unreasonable with this method, i.e., the multi-Gaussian function is spatially rotational symmetric, whereas in fact that each PSF caused by the rotation should have a curved structure towards the image center, which is not spatially rotational symmetric, e.g., the PSFs shown in the yellow and green rectangles in Fig. 3(b). Therefore, just as in [45], we propose to use the principal component analysis (PCA) to convert the measured PSFs into a linear combination of some spatially invariant

eigen-PSFs and weighting coefficient matrices, then the radial basis function (RBF) interpolation is adopted on the weighting coefficient matrices to achieve a representation of the other PSFs and reconstruct them. Theoretically, this method can model the spatially rotational PSFs more accurately. To make a fair comparison, for the method in [44], we also use the same preprocessing method in Subsection 2.3 to deal with the PAT images before they are restored with the hyper-Laplacian regularized non-blind deconvolution method [19]. For simplicity, we call the modified method of that in [44] by measurement based non-blind spatially variant deconvolution (MNBSVD) in the following subsections. Here, we should note that our research group has also proposed a similar regularized non-blind deconvolution method as MNBSVD in [45]. Since the quality of the restored image is mainly
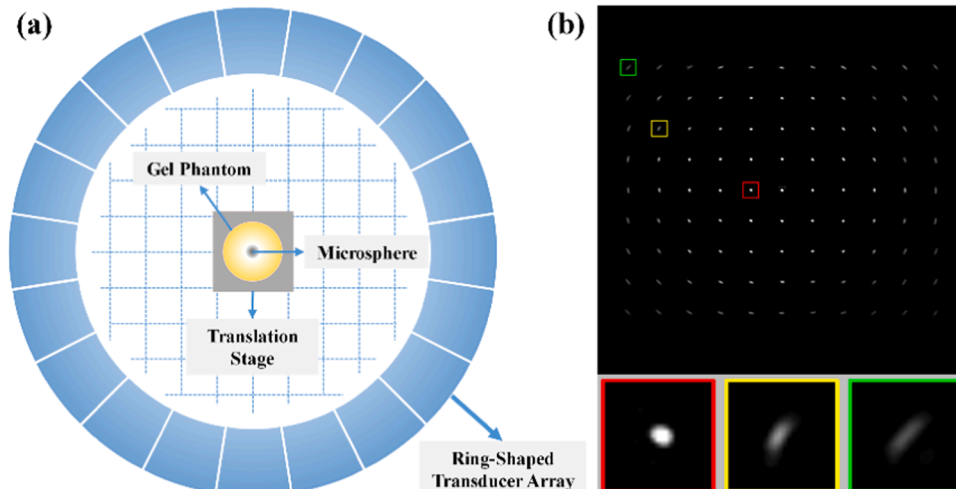
Fig. 3. PSF measurement of the ring-array PAT system. (a) The schematic diagram for measuring the PSFs. (b) The obtained PSF map.

determined by the accuracy of the measured spatially variant PSFs and there is no remarkable difference between their performances, we only take the MNBSVD method for comparison in the following parts.

3.2. Experiments based on phantoms

As we all known, an ideal imaging system should have a small point-like spatially invariant PSF at every position in the field of view. However, since the PSFs of the ring-array PAT system is spatially variant, they will have different shapes at different positions, if the proposed method can restore all of them into small point-like PSFs, its effectiveness is proved.

To measure the spatially variant PSFs of the ring-array PAT system used in our experiments, we prepare a gel phantom containing a single black microsphere with diameter of $100\mu m$, the phantom is fixed on a sample holder to avoid floating in the medium and moved with a precise translation stage to measure the PSFs at different positions in the PAT system. According to the setup of the transducer array, the theoretical resolution at the center of the PAT system is about $250.4\mu m$, thus the microsphere with diameter $100\mu m$ is small enough to ensure the measurement accuracy. The schematic diagram for measuring the PSFs is shown in Fig. 3(a) and the map of the measured PSFs is shown in Fig. 3 (b), we can see that as the distance from the center increases, the PSF spreads wider around the image center, which is consistent with the spatially variant blur caused by rotation.

Fig. 4(a) shows the same measured PSF map as in Fig. 3(b), then we use the MNBSVD and the proposed method to restore it, the results are presented in Fig. 4(b) and (c), respectively. Fig. 4(d)-(f) are the enlarged views of the contents in the red rectangles in Fig. 4(a)-(c), respectively. From these figures and the contents in the yellow rectangles we can see that both of the two methods successfully convert the original extended PSFs at all positions into small point-like PSFs, which is consistent with the above analysis and proves their effectiveness. Besides, we also extract the pixel values along the green solid line of Fig. 4(d)-(f), normalize and plot them in Fig. 4(g). We can see clearly that the extent of the point is obviously contracted, the proposed method performs as well as the MNBSVD method.

We also make another phantom which contains many randomly scattered microspheres (Fig. 5(a)) and reconstruct its PAT image with

the FBP method (Fig. 5(b)). Fig. 5(c) and (d) exhibit the results of the MNBSVD method and ours, the enlarged views of the contents in the red rectangles in Fig. 5(a)-(d) are shown in Fig. 5(e)-(h), respectively. We can see that due to the spatially rotational blur degradation, some of the microspheres are extended and stick together in Fig. 5(f). After processing it with the MNBSVD and the proposed method, the extended microspheres shrink to rounder points and can be easily distinguished from each other, as shown in the yellow rectangles in Fig. 5(f)-(h), which means the resolution is improved. We also plot the profiles of Fig. 5(f)-(h) along the green solid line, we can see that the peak values of the MNBSVD and the proposed method are much higher than the blurred. It is evident that the performance of our approach is comparable with that of the MNBSVD.

Besides the above phantoms of microspheres, we also make another one which contains some hairs for evaluation. Fig. 6(a) shows the phantom in which some of the hairs crosses over each other and Fig. 6(b) is the reconstructed PAT image with FBP. Fig. 6(c) and (d) are the restored images of the MNBSVD and our approach, respectively. The enlarged views of the contents in the red rectangles in Fig. 6(a)-(d) are shown in Fig. 6(e)-(h), respectively, from which we can see that the adjacent hairs in both of the two restored images are successfully separated. In Fig. 6(i), the profiles along the green solid line are plotted, from which we can see that the proposed method presents the interval between the two adjacent hairs better than the MNBSVD. Our result is also clearer and has more details than that of the MNBSVD.

3.3. Experiments based on in vivo biological tissues

Besides the experiments based on phantoms, we also capture PAT images of some in vivo biological tissues and evaluate the performance of the proposed method.

Fig. 7(a) shows the PAT image of the blood vessels of a mouse abdomen which contains rich details. Obviously, it is degraded by both blur and streak artifacts. Fig. 7(b) and (c) present the restored images of the MNBSVD and our method, respectively. Fig. 7(d)-(f) are the enlarged views of the contents in the red rectangles in Fig. 7(a)-(c). From the contents in the yellow rectangles we can see that our method improves the image resolution effectively and performs better than the MNBSVD. Fig. 7(g) shows the profiles along the green solid line of Fig. 7(d)-(f), we
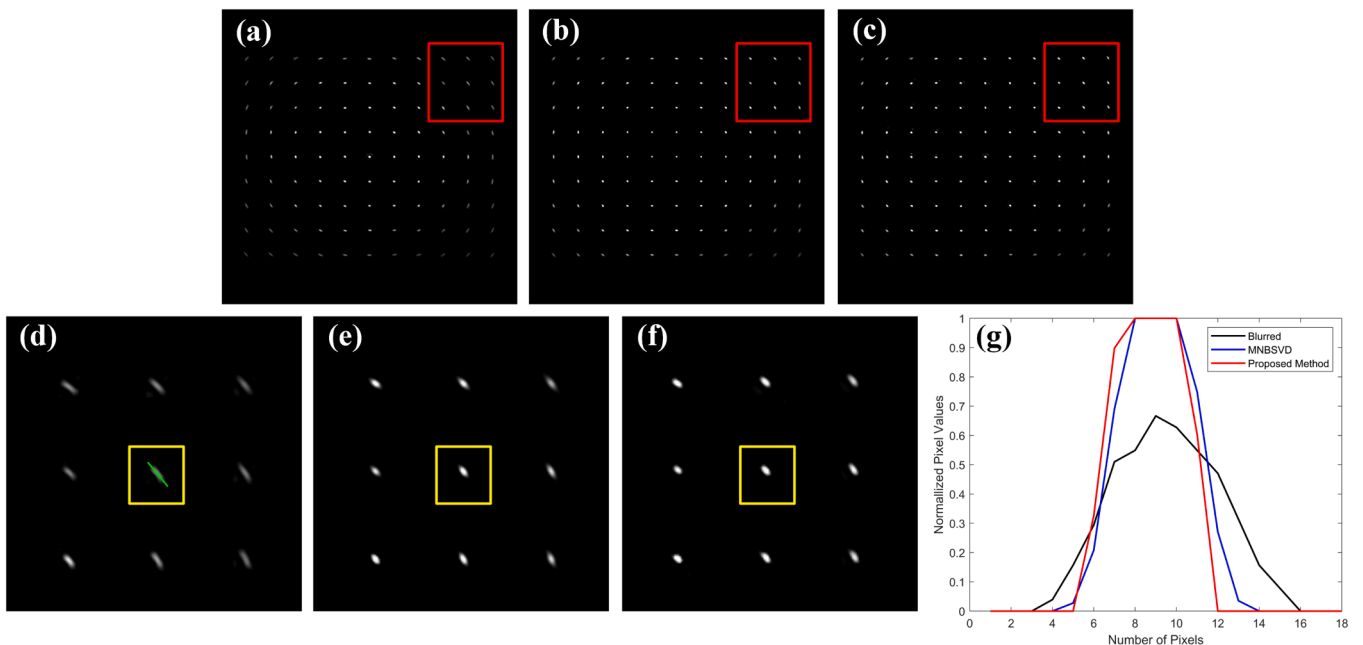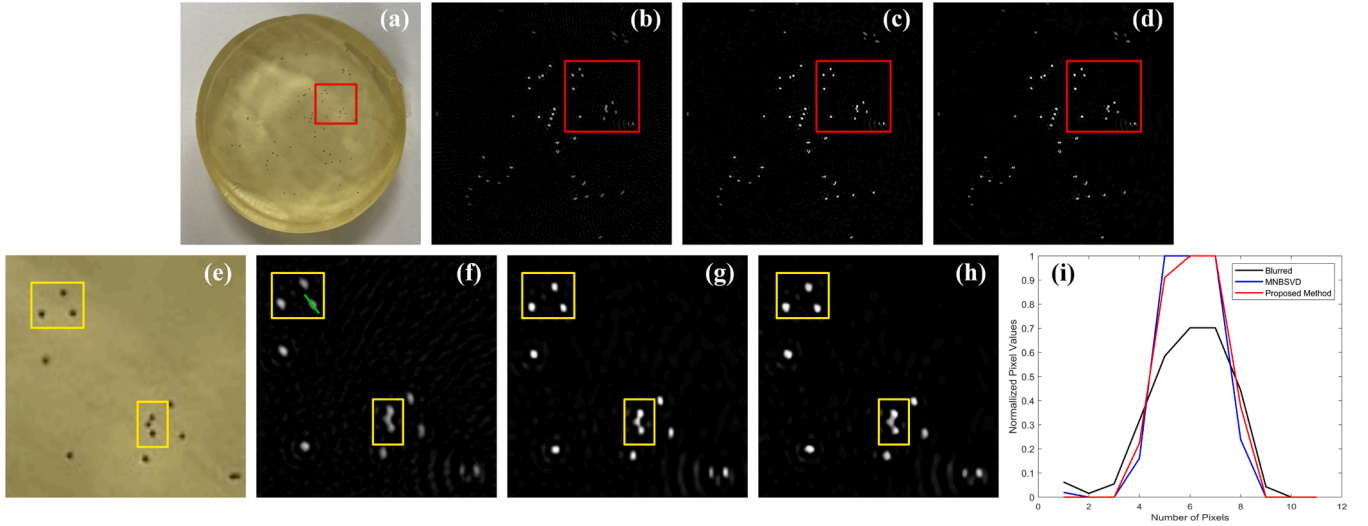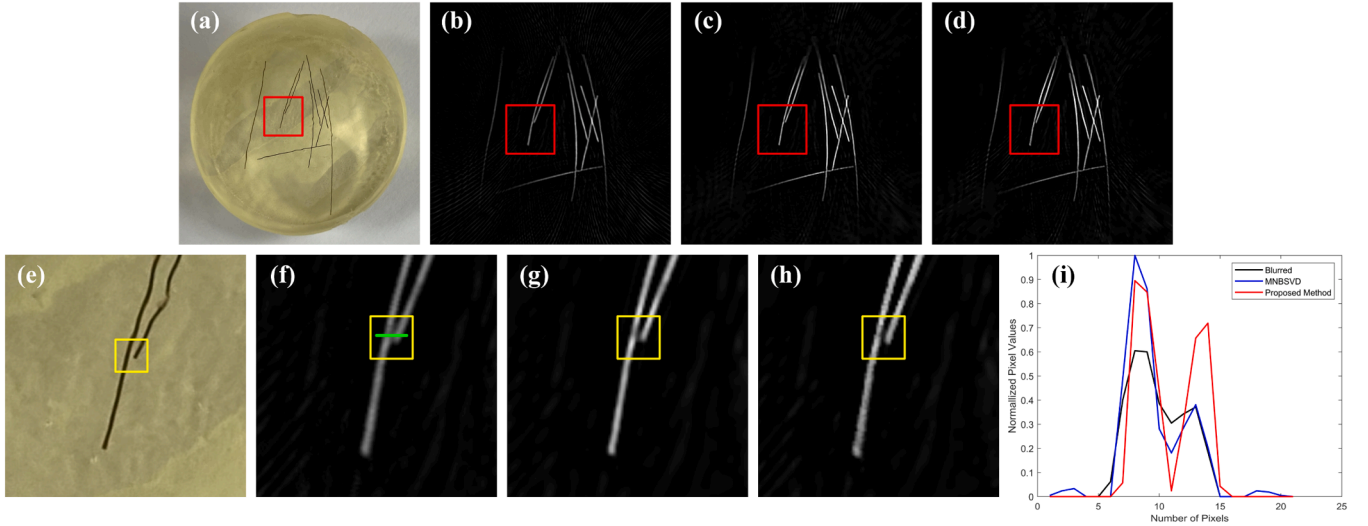

Fig. 4. Experimental results of the PSF map. (a) The measured PSF map. (b) The result of MNBSVD. (c) The result of the proposed method. (d)-(f) Enlarged views of the contents in the red rectangles in (a)-(c), respectively. (g) Normalized profiles of the pixel values of (d)-(f) along the green solid line.

Fig. 5. Experimental results of the microsphere phantom. (a) The phantom. (b) The original PAT image. (c) The result of MNBSVD. (d) The result of the proposed method. (e)-(h) Enlarged views of the contents in the red rectangles in (a)-(d), respectively. (i) Normalized profiles of the pixel values of (f)-(h) along the green solid line.

Fig. 6. Experimental results of the hair phantom. (a) The phantom. (b) The original PAT image. (c) The result of MNBSVD. (d) The result of the proposed method. (e)-(h) Enlarged views of the contents in the red rectangles in (a)-(d), respectively. (i) Normalized profiles of the pixel values of (f)-(h) along the green solid line.

can see that the proposed method reveals the change of the pixel values more clearly. Besides, most of the streak artifacts in the backgrounds are also suppressed, as pointed by the white arrows.

In Fig. 8(a), a reconstructed PAT image of a human finger is presented, which shows very evident spatially rotational blur and the backgrounds are full of radial streak artifacts. Fig. 8(b) is the restored image of the MNBSVD method, while Fig. 8(c) is result of the proposed method. The enlarged views of the contents in the red rectangles in Fig. 8(a)-(c) are shown in Fig. 8(d)-(f), respectively, it is obviously that the streak artifacts are almost completely removed as pointed by the white arrows. Further taking a comparison between the contents in the yellow rectangles in Fig. 8(e) and (f), we can see that our approach performs much better in improving the image resolution than the MNBSVD method. In Fig. 8(g), the profiles along the green solid line of different images are given, from which we can also see that the proposed method effectively removes the blur effect in the original PAT image and improves its resolution.

3.4. Quantitative evaluation of image quality improvement

Besides the visual judgment, we also adopt the image contrast to evaluate the blurred and restored images to determine how much exactly the image quality has been improved. Image contrast is an index which is used to assess the clarity of an image, whose definition is given by the following equation:

$$Contrast = \sum_{\delta} \delta(i,j)^2 P_\delta(i,j) \tag{28}$$

where i and j are indices of adjacent pixels, $\delta(i,j)$ represents the difference between the gray values of adjacent pixels, $P_\delta(i,j)$ represents the probability of $\delta(i,j)$. Since the cause of image blur is essentially neighboring pixels superimposed on each other which results in a decrease of $\delta(i,j)^2$, a blurred image will have a lower contrast than the corresponding clear image. Firstly, we calculate the contrast values of the blurred PAT images, the restored images of the MNBSVD and the proposed method in Figs. 4–8. Then we also calculate the ratios between
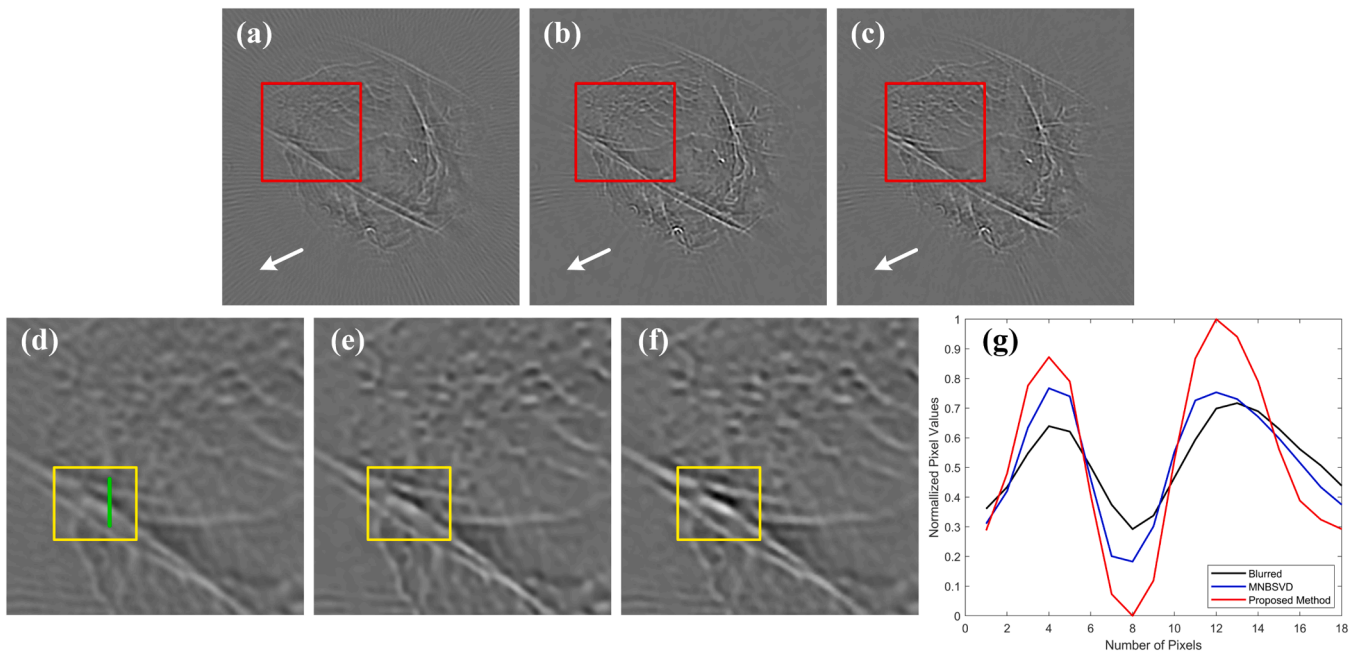
Fig. 7. Experimental results of the blood vessels of a mouse abdomen. (a) The original PAT image. (b) The result of MNBSVD. (c) The result of the proposed method. (d)-(f) Enlarged views of the contents in the red rectangles in (a)-(c), respectively. (g) Normalized profiles of the pixel values of (d)-(f) along the green solid line.
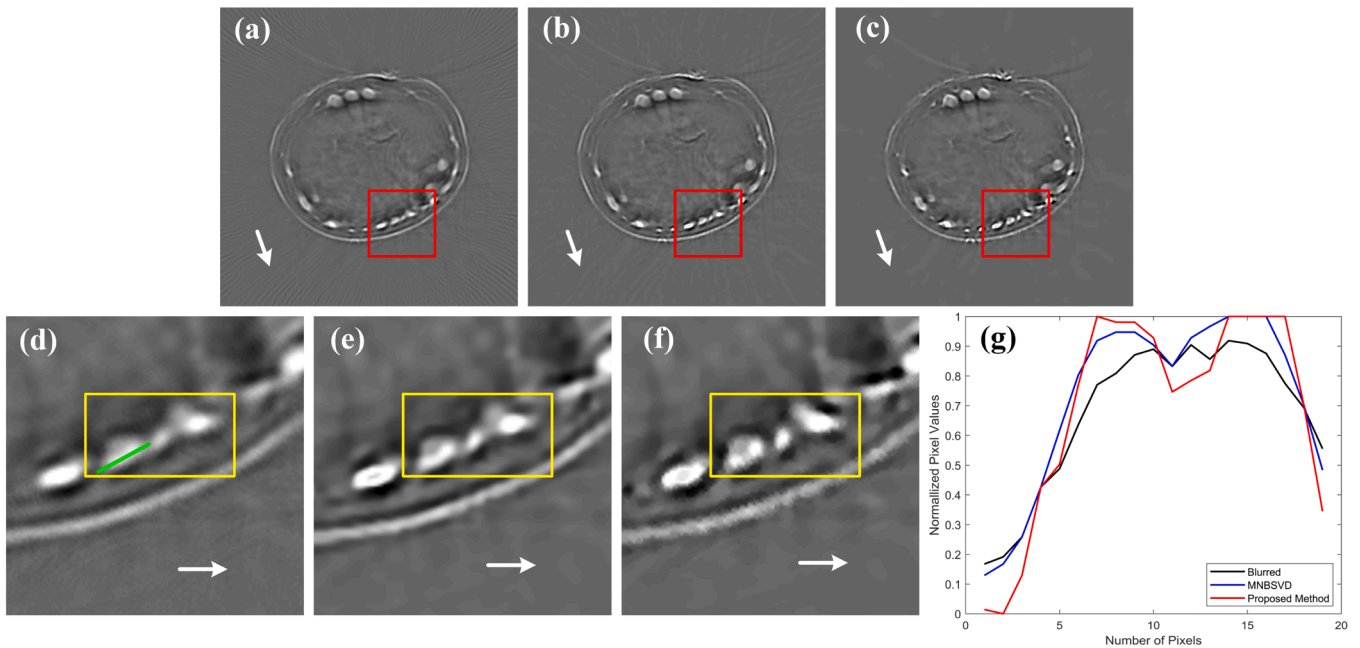

Fig. 8. Experimental results of a human finger. (a) The original PAT image. (b) The result of MNBSVD. (c) The result of the proposed method. (d)-(f) Enlarged views of the contents in the red rectangles in (a)-(c), respectively. (g) Normalized profiles of the pixel values of (d)-(f) along the green solid line.

Table 1
Image contrast values and the ratios between them.

Figure	Blurred (C_1)	MNBSVD (C_2)	Proposed (C_3)	C_2 / C_1	C_3 / C_1
Fig. 4	44.47	84.03	94.03	1.89	**2.13**
Fig. 5	33.76	52.37	48.31	**1.55**	1.43
Fig. 6	78.57	181.53	201.09	2.31	**2.56**
Fig. 7	29.38	56.14	56.88	1.91	**1.94**
Fig. 8	29.51	36.50	43.13	1.24	**1.46**

them and show the results in Table 1, where the bold font denotes the largest ratio of each row. We can see that except Fig. 5, the proposed method outperforms the MNBSVD in image quality improvement.

3.5. Computational efficiency

The above experiments and evaluations have proven the effectiveness of the proposed method in improving the quality of the PAT images. However, the computational efficiency is also an important index to assess the algorithm, here we give the implementation environment and typical running time of the proposed method.

The algorithm is programed with Matlab 2022a and run on a workstation equipped with two 10-core 20-thread CPUs whose base working frequency is 2.4 GHz. To accelerate the program, we choose to implement the image rotation on a GPU with 24 G memory. All the PAT images presented in this paper have 1000×1000 pixels, it takes about 80.4 seconds and 850.6 seconds to finish the image preprocessing and blind spatially rotational deconvolution, respectively. If the PAT image to be restored is of smaller size, e.g., 512×512 or 256×256 pixels as in most current researches, the computational time will be reduced. Table 2 gives the running time for PAT images of different sizes.

4. Discussion

4.1. Effects of image preprocessing on the restored image

Just as shown in Subsection 2.3, the streak artifacts degrade the image quality, and the role of image preprocessing is to remove them. If there is no image preprocessing, there will be two negative effects on the restored image. Firstly, the streak artifacts will be preserved in the restored image, which will degrade the image quality directly. Secondly, the accuracy of the estimated rotational PSF may be lowered due to the effect of the streak artifacts, and thus in turn degrades the quality of the restored image indirectly. We also take an example to show the result if there is no image preprocessing in Fig. 9, the degraded image to be processed is the same as Fig. 8(a). As pointed by the white and yellow arrows, the restored image without image preprocessing contains much more undesired artifacts than that of the proposed method.

4.2. Effects of EIR on image resolution degradation in our experimental PAT system

Actually, the spatial resolution of a PAT system is indeed affected by both the EIR and SIR. Theoretically, the MNBSVD method can remove the blur caused by both EIR and SIR, while our method can only remove the blur caused by SIR, thus the MNBSVD method should perform better than the proposed method, which is not consistent with the experimental results. We have analyzed the experimental configurations and give the possible explanations as follow.

Firstly, based on the parameters of the experimental system in Subsection 3.1, we can calculate the profile of the PSF caused by EIR with Eq. (29) which is given in [64] and [65], and show it by the red curve in Fig. 10.

$$h(r) = \frac{k_c^2}{2\pi^2 r}\left\{(1+0.5B)^2 j_1\left[(1+0.5B)k_c r\right] - (1-0.5B)^2 j_1\left[(1-0.5B)k_c r\right]\right\}$$

(29)

where $h(r)$ denotes the profile of the PSF caused by EIR, r is the distance from the original point, B denotes the bandwidth, $k_c = 2\pi f_c/v_s$ and f_c is the center frequency, j_1 is the first-order spherical Bessel function of the first kind.

We can see that the resolution due to the EIR is about 125.2×2=250.4μm in our experimental PAT system. We also calculate the profile of the PSF for a nearly EIR-free condition, in which the center frequency is 10 MHz and the bandwidth is extended to 200%, i.e., the passband is 0–20 MHz, as shown by the blue curve in Fig. 10. We can get that the resolution is about 61.3×2=122.6μm and this is the limit that deconvolution with EIR can reach. That means if we recognize 122.6μm

as the minimum size of a distinguishable point in a nearly EIR-free PAT system, then the blur extent caused by EIR in our experimental system is only about 250.4/122.6=2.04 points, thus the blur effect caused by EIR in our experiments is very weak compared with that of SIR. Besides, the hyper-Laplacian regularized non-blind deconvolution method that is adopted in MNBSVD may smooth image details while suppress the undesired artifacts, which may also slightly affect the improvement of resolution. These two factors make the deconvolution with EIR only have very small effects on resolution improvement in our experiments, and that is why the proposed method can only remove the blur effect caused by SIR, but it can perform as well as the MNBSVD method.

Since the PSF caused by EIR is spatially invariant, in other PAT system where the EIR evidently degrades the resolution, e.g., the center frequency is too low and the bandwidth is narrow, we can easily calculate or only take one measurement at the center of the ring-shaped transducer array to obtain the EIR caused PSF, and use some spatially invariant non-blind deconvolution methods to further remove the corresponding blur effect. This modification can still make the performance of the proposed method be comparable with that of the MNBSVD method.

### 4.3. Effects of different regularizations on the restored image

According to the optimization theory, the regularization methods can be roughly divided into two categories, i.e., the quadratic regularization and the sparse regularization. Both of them are used to improve the ill-posedness of the inverse problem.

The Tikhonov regularization is a typical quadratic regularization method, the advantage is that it derives quadratic optimization problems which can be solved efficiently. However, it also has an obvious disadvantage, i.e., the edges of the intermediately restored image in the blind deconvolution process tend to be overly smoothed. Since the preservation of sharp image edges is very important for PSF estimation in blind image deconvolution, the Tikhonov regularization is not suitable for regularizing the image in blind image deconvolution. In contrast, the TV regularization is a very simple and commonly used sparse regularization method for the image, and there have been some fast optimization methods for solving the TV regularization problem, e. g., the method adopted in our research [66]. Although the computational efficiency of these methods is still lower than that for solving the Tikhonov regularization problem, the TV regularization can preserve many sharp image edges during the blind deconvolution process, which is very beneficial for promoting the accuracy of PSF estimation. This is why we use TV regularization in the **x**-problem, i.e., regularize the image in the algorithm. We can certainly use other sparse regularization methods for the **x**-problem, e.g., the L_1-norm of image gradient regularization [67], or more sophisticated hybrid TV-L_0 regularization [68]. Just as shown in the following Fig. 11 (a)-(c) and (e)-(g), the Tikhonov regularization cannot achieve satisfactory restored image, while the restored images of L_1-norm of image gradient regularization and TV-L_0 regularization are very close to that of the TV regularization in Fig. 8(c) and (f). Although adopting more complicated regularization methods may improve the quality of the result, the computational efficiency may be also lowered.

For the regularization of **w**-problem, just as demonstrated above, the accuracy of the estimated **w** is mainly determined by the sharp edges of the intermediately restored image during blind deconvolution, thus we can use either quadratic regularization or sparse regularization for it, there will be no obvious difference on the final result. Just as shown in the following Fig. 11 (d) and (h), we can see that when using the TV regularization in the **w**-problem, the restored image is of similar quality as that using the Tikhonov regularization (i.e., Fig. 8(c) and (f)). However, since the Tikhonov regularization problem is easy to be solved, we choose it to regularize the rotational PSF **w** in our algorithm to promote the computational efficiency.

Table 2
Running time for restoring PAT images of different sizes.

| Image size	Time for image preprocessing	Time for blind spatially rotational deconvolution
256×256	10.7 s	518.6 s
512×512	36.6 s	638.0 s
1000×1000	80.4 s	850.6 s
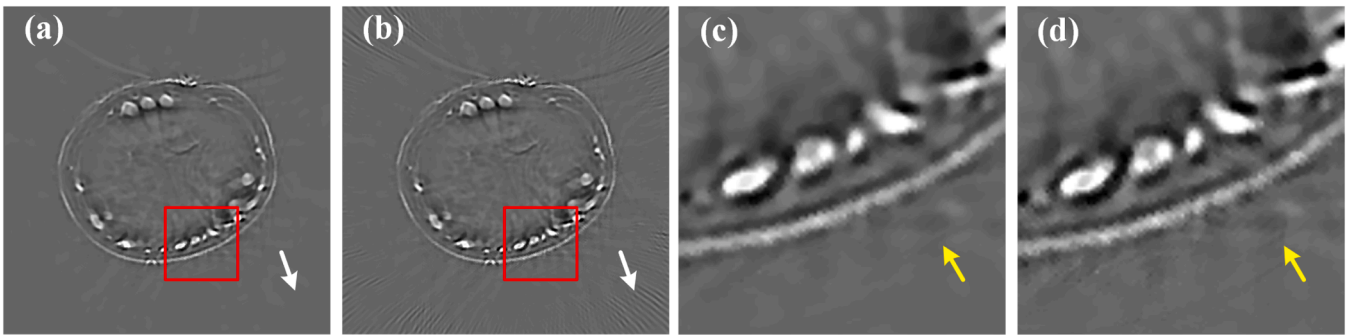
Fig. 9. Experimental results of a human finger. (a) The result of the proposed method in Fig. 8(c). (b) The result without image preprocessing. (c)-(d) Enlarged views of the contents in the red rectangles in (a)-(b), respectively.
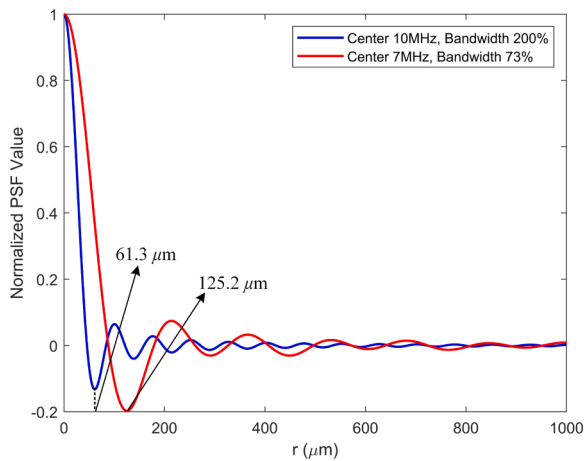
Fig. 10. The profiles of the PSFs due to different bandwidths.

5. Conclusions

In this paper, we propose a new concept, i.e., spatially rotational convolution to formulate the spatially rotational blur effect in the image obtained from a ring-array PAT system, where the degradation process is expressed by rotating the clear image with several equally spaced degrees and calculating the weighted sum. Then we propose a regularized blind spatially rotational deconvolution problem model based on it and design an efficient alternating minimization algorithm to solve it. In order to remove the spatially rotational blur and streak artifacts in the PAT image effectively, we propose a two stage restoration scheme. Firstly, we rotate the PAT image clockwise and counterclockwise with a certain degree around the image center and calculate the average image to counteract the streak artifacts, then we deconvolve it with the proposed non-blind spatially rotational deconvolution method to eliminate the slight blur caused by the rotation and averaging operation, and afterwards we adopt the proposed blind spatially rotational deconvolution algorithm on the result to achieve the final restored image. Experimental results show that our approach can achieve restored image of very high quality which is competitive with the state of the art non-blind spatially variant deconvolution method, and does not need any auxiliary devices for PSF measurement. The research is expected to provide a reference
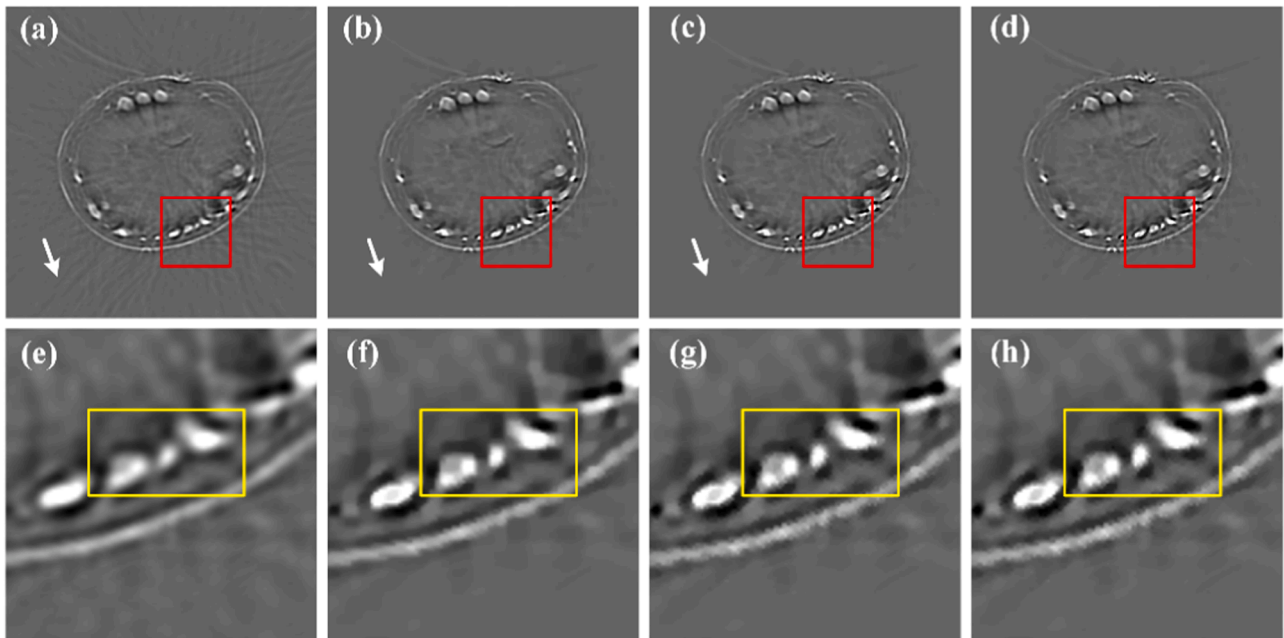
Fig. 11. Experimental results of different regularizations. (a) Tikhonov regularization for the **x**-problem. (b) L_1-norm of image gradient regularization for the **x**-problem. (c) Hybrid TV- L_0 regularization for the **x**-problem. (d) TV regularizations for both the **x**-problem and **w**-problem. (e)-(h) Enlarged views of the contents in the red rectangles in (a)-(d), respectively.

guide for improving the performance of ring-array PAT systems.

CRediT authorship contribution statement

Shuyin Tao: Writing – review & editing. **Chao Tian:** Methodology, Conceptualization. **Dan Xie:** Software. **Yanli Zhang:** Software. **Wende Dong:** Writing – original draft, Methodology. **Chenlong Zhu:** Formal analysis.

Declaration of Competing Interest

The authors declare that they have no known competing financial interests or personal relationships that could have appeared to influence the work reported in this paper.

Data availability

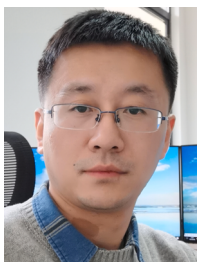Data will be made available on request.

Acknowledgments

References

[1] L.V. Wang, S. Hu, Photoacoustic tomography: in vivo imaging from organelles to organs, Science 335 (6075) (2012) 1458–1462.

[2] L.V. Wang, J. Yao, A practical guide to photoacoustic tomography in the life sciences, Nat. Methods 13 (8) (2016) 627–638.

[3] B.E. Treeby, E.Z. Zhang, B.T. Cox, Photoacoustic tomography in absorbing acoustic media using time reversal, Inverse Probl. 26 (11) (2010).

[4] Y. Xu, L.H.V. Wang, Time reversal and its application to tomography with diffracting sources, Phys. Rev. Lett. 92 (3) (2004).

[5] M.H. Xu, L.H.V. Wang, Pulsed-microwave-induced thermoacoustic tomography: Filtered backprojection in a circular measurement configuration, Med. Phys. 29 (8) (2002) 1661–1669.

[6] M.H. Xu, L.H.V. Wang, Universal back-projection algorithm for photoacoustic computed tomography, Phys. Rev. E 71 (1) (2005).

[7] G. Paltauf, J.A. Viator, S.A. Prahl, S.L. Jacques, Iterative reconstruction algorithm for optoacoustic imaging, J. Acoust. Soc. Am. 112 (4) (2002) 1536–1544.

[8] K. Wang, R. Su, A.A. Oraevsky, M.A. Anastasio, Investigation of iterative image reconstruction in three-dimensional optoacoustic tomography, Phys. Med. Biol. 57 (17) (2012) 5399–5423.

[9] C. Tian, W. Zhang, A. Mordovanakis, X. Wang, Y.M. Paulus, Noninvasive chorioretinal imaging in living rabbits using integrated photoacoustic microscopy and optical coherence tomography, Opt. Express 25 (14) (2017) 15947–15955.

[10] A.B.E. Attia, et al., A review of clinical photoacoustic imaging: current and future trends, Photoacoustics 16 (2019).

[11] C. Tian, C. Zhang, H. Zhang, D. Xie, Y. Jin, Spatial resolution in photoacoustic computed tomography, Rep. Prog. Phys. 84 (3) (2021).

[12] L.I. Rudin, S. Osher, E. Fatemi, Nonlinear total variation based noise removal algorithms, Phys. D. 60 (1-4) (1992) 259–268.

[13] T.F. Chan, W. Chiu-Kwong, Total variation blind deconvolution, IEEE Trans. Image Process. 7 (3) (1998) 370–375.

[14] J.M. Bioucas-Dias, M.A.T. Figueiredo, J.P. Oliveira, Total variation-based image deconvolution: a majorization-minimization approach, IEEE Int. Conf. Acoust., Speech Signal Process. 2006 (2006).

[15] A.N. Tikhonov, On the stability of inverse problems, Proc. Dok. Akad. Nauk SSSR 1943 (1943).

[16] A.N. Tikhonov, A.V. Goncharsky, V.V. Stepanov, A.G. Yagola, Kluwer Academic Publishers, Numer. Methods Solut. Ill. -posed Probl. (1995).

[17] J.M. Bardsley, N. Laobeul, Tikhonov regularized Poisson likelihood estimation: theoretical justification and a computational method, Inverse Probl. Sci. Eng. 16 (2) (2008) 199–215.

[18] A. Levin, R. Fergus, F. Durand, W.T. Freeman, Image and depth from a conventional camera with a coded aperture, ACM Trans. Graph. 26 (3) (2007).

[19] D. Krishnan, R. Fergus, Fast image deconvolution using hyper-Laplacian priors, Adv. Neural Inf. Process. Syst. 22 (2009) 1–9.

[20] W. Dong, H. Feng, Z. Xu, Q. Li, Multi-frame blind deconvolution using sparse priors, Opt. Commun. 285 (9) (2012) 2276–2288.

[21] L. Xu, S. Zheng, J. Jia, Unnatural L_0 sparse representation for natural image deblurring, IEEE Conf. Comput. Vis. Pattern Recognit. 2013 (2013).

[22] J. Pan, Z. Hu, Z. Su, M.-H. Yang, L_0-regularized intensity and gradient prior for deblurring text images and beyond, IEEE Trans. Pattern Anal. Mach. Intell. 39 (2) (2017) 342–355.

[23] S. Tao, W. Dong, J. Xu, J. Lu, G. Xu, Y. Chen, An adaptive two phase blind image deconvolution algorithm for an iterative regularization model, J. Vis. Commun. Image Represent. 81 (2021).

[24] J. Liu, M. Yan, T. Zeng, Surface-aware blind image deblurring, IEEE Trans. Pattern Anal. Mach. Intell. 43 (3) (2021) 1041–1055.

[25] W. Dong, S. Tao, G. Xu, Y. Chen, Blind deconvolution for poissonian blurred image with total variation and L_0-norm gradient regularizations, IEEE Trans. Image Process. 30 (2021) 1030–1043.

[26] Y.-W. Tai, H. Du, M.S. Brown, S. Lin, Correction of spatially varying image and video motion blur using a hybrid camera, IEEE Trans. Pattern Anal. Mach. Intell. 32 (6) (2010) 1012–1028.

[27] N. Joshi, S.B. Kang, C.L. Zitnick, R. Szeliski, Image deblurring using inertial measurement sensors, ACM Trans. Graph. 29 (4) (2010).

[28] A. Gupta, N. Joshi, C.L. Zitnick, M. Cohen, B. Curless, Single image deblurring using motion density functions, Eur. Conf. Comput. Vis. (2010) 2010.

[29] O. Whyte, J. Sivic, A. Zisserman, J. Ponce, Non-uniform deblurring for shaken images, Int. J. Comput. Vis. 98 (2) (2012) 168–186.

[30] C.S. Vijay, C. Paramanand, A.N. Rajagopalan, R. Chellappa, Non-uniform deblurring in HDR image reconstruction, IEEE Trans. Image Process. 22 (10) (2013) 3739–3750.

[31] X. Yu, F. Xu, S. Zhang, L. Zhang, Efficient patch-wise non-uniform deblurring for a single image, IEEE Trans. Multimed. 16 (6) (2014) 1510–1524.

[32] M.-L. Li, C.-C. Cheng, Reconstruction of photoacoustic tomography with finite-aperture detectors: deconvolution of the spatial impulse response, Conf. Photons Ultrasound - Imaging Sens. 2010 (2010).

[33] T. Lu, Y. Wang, J. Li, J. Prakash, F. Gao, V. Ntziachristos, Full-frequency correction of spatial impulse response in back-projection scheme using space-variant filtering for optoacoustic mesoscopy, Photoacoustics 19 (2020).

[34] N.A. Rejesh, H. Pullagurla, M. Pramanik, Deconvolution-based deblurring of reconstructed images in photoacoustic/thermoacoustic tomography, J. Opt. Soc. Am. a-Opt. Image Sci. Vision 30 (10) (2013) 1994–2001.

[35] K. Wang, S.A. Ermilov, R. Su, H.-P. Brecht, A.A. Oraevsky, M.A. Anastasio, An imaging model incorporating ultrasonic transducer properties for three-dimensional optoacoustic tomography, IEEE Trans. Image Process. 30 (2) (2011) 203–214.

[36] C. Zhang, Y. Wang, Deconvolution reconstruction of full-view and limited-view photoacoustic tomography: a simulation study, J. Opt. Soc. Am. a-Opt. Image Sci. Vis. 25 (10) (2008) 2436–2443.

[37] C. Zhang, C. Li, L.V. Wang, Fast and robust deconvolution-based image reconstruction for photoacoustic tomography in circular geometry: experimental validation, IEEE Photonics J. 2 (1) (2010) 57–66.

[38] U.A.T. Hofmann, W. Li, X.L. Dean-Ben, P. Subochev, H. Estrada, D. Razansky, Enhancing optoacoustic mesoscopy through calibration-based iterative reconstruction, Photoacoustics 28 (2022).

[39] K.B. Chowdhury, J. Prakash, A. Karlas, D. Jüstel, V. Ntziachristos, A synthetic total impulse response characterization method for correction of hand-held optoacoustic images, IEEE Trans. Med. Imaging 39 (10) (2020) 3218–3230.

[40] T. Jetzfellner, V. Ntziachristos, Performance of blind decovolution in optoacoustic tomography, J. Innov. Opt. Health Sci. 4 (4 2011) 385–393.

[41] J. Chen, R. Lin, H. Wang, J. Meng, H. Zheng, L. Song, Blind-deconvolution optical-resolution photoacoustic microscopy in vivo, Opt. Express 21 (6) (2013) 7316–7327.

[42] X. Song, L. Song, A. Chen, J. Wei, Deconvolution optical-resolution photoacoustic microscope for high - resolution imaging of brain, SPIE Future Sens. Technol. Conf. 2020. (2020).

[43] D. Xie, Q. Li, Q. Gao, W. Song, H.F. Zhang, X. Yuan, In vivo blind-deconvolution photoacoustic ophthalmoscopy with total variation regularization, J. Biophotonics 11 (9) (2018).

[44] L. Qi, et al., Photoacoustic tomography image restoration with measured spatially variant point spread functions, IEEE Trans. Med. Imaging 40 (9) (2021) 2318–2328.

[45] D. Xie, W. Dong, J. Zheng, C. Tian, Spatially-variant image deconvolution for photoacoustic tomography, Opt. Express 31 (13) (2023) 21641–21657.

[46] J. Meng, L.V. Wang, L. Ying, D. Liang, L. Song, Compressed-sensing photoacoustic computed tomography in vivo with partially known support, Opt. Express 20 (15) (2012) 16510–16523.

[47] Y. Zhang, Y. Wang, C. Zhang, Total variation based gradient descent algorithm for sparse-view photoacoustic image reconstruction, Ultrasonics 52 (8) (2012) 1046–1055.

[48] Y. Han, S. Tzoumas, A. Nunes, V. Ntziachristos, A. Rosenthal, Sparsity-based acoustic inversion in cross-sectional multiscale optoacoustic imaging, Med. Phys. 42 (9) (2015) 5444–5452.

[49] Y. Han, L. Ding, X.L.D. Ben, D. Razansky, J. Prakash, V. Ntziachristos, Three-dimensional optoacoustic reconstruction using fast sparse representation, Opt. Lett. 42 (5) (2017) 979–982.

[50] G. Paltauf, R. Nuster, P. Burgholzer, Weight factors for limited angle photoacoustic tomography, Phys. Med. Biol. 54 (11) (2009) 3303–3314.

[51] C. Cai, X. Wang, K. Si, J. Qian, J. Luo, C. Ma, Streak artifact suppression in photoacoustic computed tomography using adaptive back projection, Biomed. Opt. Express 10 (9) (2019) 4803–4814.

[52] J. Groehl, M. Schellenberg, K. Dreher, L. Maier-Hein, Deep learning for biomedical photoacoustic imaging: A review, Photoacoustics 22 (2021).

[53] S. Antholzer, M. Haltmeier, J. Schwab, Deep learning for photoacoustic tomography from sparse data, Inverse Probl. Sci. Eng. 27 (7) (2019) 987–1005.

[54] N. Davoudi, X.L. Deán-Ben, D. Razansky, Deep learning optoacoustic tomography with sparse data, Nat. Mach. Intell. 1 (10) (2019) 453–460.

[55] H. Shahid, A. Khalid, X. Liu, M. Irfan, D. Ta, A deep learning approach for the photoacoustic tomography recovery from undersampled measurements, Front. Neurosci. 15 (2021).

[56] N. Davoudi, B. Lafci, A. Özbek, X.L. Deán-Ben, D. Razansky, Deep learning of image- and time-domain data enhances the visibility of structures in optoacoustic tomography, Opt. Lett. 46 (13) (2021) 3029–3032.

[57] T. Vu, M. Li, H. Humayun, Y. Zhou, J. Yao, A generative adversarial network for artifact removal in photoacoustic computed tomography with a linear-array transducer, Exp. Biol. Med. 245 (7) (2020) 597–605.

[58] H. Shahid, A. Khalid, Y. Yue, X. Liu, D. Ta, Feasibility of a generative adversarial network for artifact removal in experimental photoacoustic imaging, Ultrasound Med. Biol. 48 (8) (2022) 1628–1643.

[59] T. Lu, T. Chen, F. Gao, B. Sun, V. Ntziachristos, J. Li, LV-GAN: A deep learning approach for limited-view optoacoustic imaging based on hybrid datasets, J. Biophotonics 14 (2) (2021).

[60] H. Shan, G. Wang, Y. Yang, Accelerated correction of reflection artifacts by deep neural networks in photoacoustic tomography, Appl. Sci. -Basel 9 (13) (2019).

[61] P. Rajendran, M. Pramanik, Deep-learning-based multi-transducer photoacoustic tomography imaging without radius calibration, Opt. Lett. 46 (18) (2021) 4510–4513.

[62] S. Jeon, C. Kim, Deep learning-based speed of sound aberration correction in photoacoustic images, Conf. Photons Ultrasound - Imaging Sens. (2020) 2020.

[63] K. Tang, et al., Learning spatially variant degradation for unsupervised blind photoacoustic tomography image restoration, Photoacoustics 32 (2023) 100536.

[64] M.H. Xu, L.V. Wang, Analytic explanation of spatial resolution related to bandwidth and detector aperture size in thermoacoustic or photoacoustic reconstruction, Phys. Rev. E 67 (5) (2003).

[65] C. Tian, M. Pei, K. Shen, S. Liu, Z. Hu, T. Feng, Impact of system factors on the performance of photoacoustic tomography scanners, Phys. Rev. Appl. 13 (1) (2020).

[66] Y.L. Wang, J.F. Yang, W.T. Yin, Y. Zhang, A new alternating minimization algorithm for total variation image reconstruction, SIAM J. Imaging Sci. 1 (3) (2008) 248–272.

[67] M. Elad, Sparse and redundant representations: from theory to applications in signal and image processing, Springer, 2010.

[68] S. Tao, W. Dong, J. Xu, J. Lu, G. Xu, Y. Chen, An adaptive two phase blind image deconvolution algorithm for an iterative regularization model, J. Vis. Commun. Image Represent. 81 (2021).

Dan Xie obtained her bachelor degree from Nanjing University of Posts and Telecommunications in 2020, then obtained her master's degree in the University of Science and technology of China in 2023. Her research interests focus on image restoration and image reconstruction.

Yanli Zhang is a master student at the College of Automation Engineering, Nanjing University of Aeronautics and Astronautics. She obtained her B.S. degree in Measurement and Control Technology and Instruments from Xi'an Shiyou University in 2023. Her research interests are on photoacoustic tomography and deep learning.
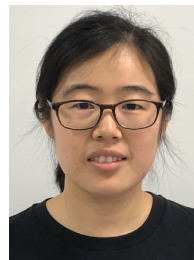
Shuyin Tao is a lecturer in the School of Computer Science and Engineering, Nanjing University of Science and Technology. She obtained his B.S. degree and PhD degree in Optical Engineering from Zhejiang University in 2009 and 2014, respectively. Her research interests focus on image dehazing, image enhancement.

Chao Tian is a professor at the School of Engineering Science, University of Science and Technology of China. He received the B.S. degree in Electrical Engineering and the PhD degree in Optical Engineering from Zhejiang University, Hangzhou, China. From 2013–2017, he worked as a Post-Doctoral Research Fellow at the University of Michigan, Ann Arbor. He is a Senior Member of Optica and a member of IEEE and SPIE. His research interests focus on biomedical imaging and image processing.

Wende Dong is an associate researcher in the College of Automation Engineering, Nanjing University of Aeronautics and Astronautics. He obtained his B.S. degree and PhD degree in Optical Engineering from Zhejiang University in 2008 and 2013, respectively. His research interests focus on image restoration, deep learning.


Chenlong Zhu is a master student in the College of Automation Engineering, Nanjing University of Aeronautics and Astronautics. He obtained his B.S. degree in Electrical Engineering and Automation from China Jiliang University in 2021. His research interests focus on image restoration and deep learning.